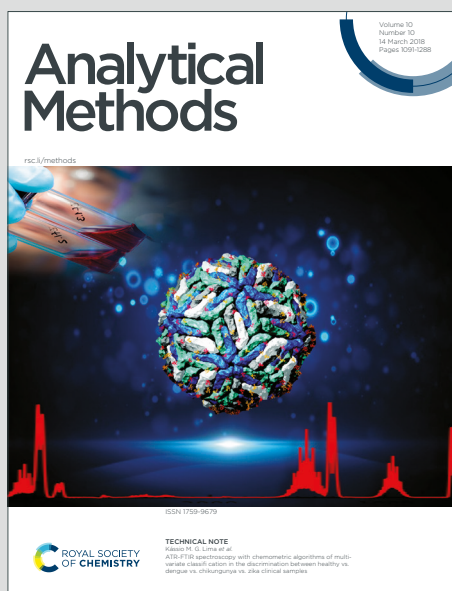


# Analytical Methods

Accepted Manuscript

This article can be cited before page numbers have been issued, to do this please use: B. B. BANKOLU, *Anal. Methods*, 2026, DOI: 10.1039/D6AY00590J.



This is an Accepted Manuscript, which has been through the Royal Society of Chemistry peer review process and has been accepted for publication.

Accepted Manuscripts are published online shortly after acceptance, before technical editing, formatting and proof reading. Using this free service, authors can make their results available to the community, in citable form, before we publish the edited article. We will replace this Accepted Manuscript with the edited and formatted Advance Article as soon as it is available.

You can find more information about Accepted Manuscripts in the [Information for Authors](#).

Please note that technical editing may introduce minor changes to the text and/or graphics, which may alter content. The journal's standard [Terms & Conditions](#) and the [Ethical guidelines](#) still apply. In no event shall the Royal Society of Chemistry be held responsible for any errors or omissions in this Accepted Manuscript or any consequences arising from the use of any information it contains.

**Quartz crystal microbalance determination of acephate based on molecularly imprinted polymer and sulphur doped copper ferrites**

View Article Online  
DOI: 10.1039/D6AY00590J

Bahar Bankoğlu Yola

*Department of Engineering Basic Sciences, Faculty of Engineering and Natural Sciences, Gaziantep Islam Science and Technology University, Gaziantep, 27260, Türkiye*

*Correspondence: bahar.bankoghuyola@gibtu.edu.tr; Tel.: +90-3429097500; Fax: 08502589800*

Analytical Methods Accepted Manuscript

1  
2  
3  
4  
5  
6  
7  
8  
9  
10  
11  
12  
13  
14  
15  
16  
17  
18  
19  
20  
21  
22  
23  
24  
25  
26  
27  
28  
29  
30  
31  
32  
33  
34  
35  
36  
37  
38  
39  
40  
41  
42  
43  
44  
45  
46  
47  
48  
49  
50  
51  
52  
53  
54  
55  
56  
57  
58  
59  
60

Downloaded on 04 May 2026 09:32:37 PM  
This article is licensed under a Creative Commons Attribution-NonCommercial 3.0 Unported Licence.



## ABSTRACT

View Article Online  
DOI: 10.1039/D6AY00590J

Acephate (ACE), an effective systemic insecticide, plays a significant role in agricultural pest control. For many decades, this compound can be used to manage various insect infestations in the crops, contributing to healthier yields. Hence, the detection of ACE serves as a critical indicator, signaling potential environmental degradation, public health risks, and economic challenges, thereby prompting necessary policy adjustments. The sulphur-doped copper ferrites (S@CuFe<sub>2</sub>O<sub>4</sub>) were initially synthesized through a hydrothermal treatment process. Subsequently, quartz crystal microbalance (QCM) chips incorporating S@CuFe<sub>2</sub>O<sub>4</sub> were fabricated. This fabrication was accomplished by providing the inherent interaction between the gold surface of QCM chip and the sulphur component present within S@CuFe<sub>2</sub>O<sub>4</sub> nanomaterial. A molecularly imprinted QCM sensor based on S@CuFe<sub>2</sub>O<sub>4</sub> was developed by a UV polymerization technique. This sophisticated fabrication process involved in the integration of methacryloylamidoglutamic acid (MAGA) as the monomer and N,N'-azobisisobutyronitrile (AIBN) which served as the crucial initiator. This innovative sensor exhibited a linear response range, spanning from 1.0×10<sup>-9</sup> to 1.0×10<sup>-8</sup> mol L<sup>-1</sup>. Furthermore, its sensitivity was remarkable, achieving a low limit of detection (LOD) at 3.30×10<sup>-10</sup> mol L<sup>-1</sup>. The newly developed QCM sensor was effectively utilized for measurements in real apple juice samples, demonstrating high recovery rates. Additionally, an investigation was conducted to assess the sensor's selectivity, evaluate its repeatability and stability, and confirm its reproducibility.

*Keywords:* Acephate; Quartz crystal microbalance; Copper ferrites; Molecularly imprinting polymers

## 1. Introduction

View Article Online  
DOI: 10.1039/D6AY00590J

With the world's population expanding rapidly, there's an increasing need to obtain a sufficient food supply. This critical demand is a significant global concern, particularly regarding the application of various agrochemicals including herbicides, pesticides, and insecticides. Among these, chemical insecticides are favored in agricultural practices owing to their affordability and considerable efficacy. ACE, a harmful broad-spectrum insecticide, exerts its lethal effect by inhibiting acetylcholinesterase. This inhibition leads to an accumulation of acetylcholine and the heightened cholinergic activity within the affected organism. Consequently, ACE poses a significant risk not only to pests but also to humans<sup>1, 2</sup>. Although ACE demonstrates dependable effectiveness against numerous insect species, direct inhalation, dermal contact, or the consumption of vegetables with its excessive residues can cause severe health consequences such as sciatic nerve damage, milder leukocytosis, and cancer<sup>3</sup>. Thus, ACE analysis in foods is significant for the well-being of both the public and the environment. The accurate and sensitive detection of insecticides is crucial, prompting researchers investigate some analytical methodologies such as HPLC<sup>4</sup> and LC-MS<sup>5</sup>. Additionally, the electrochemical analytical techniques<sup>6</sup> offer sensitive detection capabilities, while enzyme-based biological sensing techniques provide an alternative method for identifying biological interactions<sup>7</sup>. However, these techniques have some disadvantages. For example; they often require highly skilled laboratory technicians, demand considerable time for sample preparation, and involve the use of costly instrumentation. Thus, more sensitive, accurate, selective, and reliable methods are gaining prominence in the field of food analysis.

Spinel ferrites,  $M^{2+} M_2^{3+}O_4$  compounds represented by the formula  $MFe_2O_4$  (where M can be Zn, Mn, Ni, Cu, etc.), have garnered significant interest due to their utility as catalysts<sup>8, 9</sup>. Ferrite composition and crystalline structure are crucial factors that influence their adsorption capabilities, which are intricately linked to their specific morphology. Among

1  
2  
3  
4  
5  
6  
7  
8  
9  
10  
11  
12  
13  
14  
15  
16  
17  
18  
19  
20  
21  
22  
23  
24  
25  
26  
27  
28  
29  
30  
31  
32  
33  
34  
35  
36  
37  
38  
39  
40  
41  
42  
43  
44  
45  
46  
47  
48  
49  
50  
51  
52  
53  
54  
55  
56  
57  
58  
59  
60

Downloaded on 04/20/2018 8:32:37 PM  
This article is licensed under a Creative Commons Attribution-NonCommercial 3.0 Unported Licence.



these,  $\text{CuFe}_2\text{O}_4$ , a spinel-type material, is highly appealing for catalysis reactions due to its narrow band gap, robust chemical stability, and impressive visible light activity. Furthermore, its low toxicity, cost-effectiveness, versatile nature, and excellent recyclability enhance its attractiveness for such applications<sup>10</sup>. A range of techniques, including sol-gel, solid-state reaction, and coprecipitation, have been documented for synthesizing spinel ferrite microstructures. Among these, the hydrothermal method is the preferred approach due to its superior versatility, uniformity, purity, and ease of synthesis<sup>11</sup>. Despite its advantages, enhancing the effectiveness of  $\text{CuFe}_2\text{O}_4$  is crucial due to the rapid recombination of photogenerated charge carriers. To boost its catalytic efficiencies, doping with various metals and non-metals is a favored strategy<sup>12</sup>. Furthermore, due to the significant difference in size and electronegativity between oxygen and sulphur, the sulphur dopants improve the optical and electrical properties of semiconductor oxides<sup>13</sup>.

Molecular imprinting is an advanced, three-stage polymer fabrication technique. In this process, functional monomers initially form a complex with a target molecule through either covalent or non-covalent interactions. This complex is then polymerized, and the subsequent removal of the target molecule using a suitable desorption solvent yields selective polymeric structures. These polymeric structures possess the remarkable ability to recognize the template molecule. Hence, molecularly imprinted polymers (MIPs) offer several benefits, including easy preparation, cost-effectiveness, high selectivity and sensitivity, and robust durability, making them invaluable tools in modern food safety analyses<sup>14-16</sup>. MIPs-based sensors offer a highly adaptable, stable, and cost-effective approach to specific molecular recognition, which is significant for advancements in diagnostics, environmental protection, and quality control.<sup>17-25</sup>

This study presented a novel approach for the sensitive detection of ACE insecticide, integrating MIPs integrated with sulphur doped copper ferrites. Specifically, a high-sensitivity

sensor was developed by combining the high selectivity properties of MIPs with the high adsorption properties of S@CuFe<sub>2</sub>O<sub>4</sub> nanomaterial. The research involved first synthesizing the sulphur doped copper ferrites through a hydrothermal treatment. Following this, a QCM sensor was developed using sulphur doped copper ferrites coated with MIPs. This innovative sensor was then successfully utilized for the precise determination of ACE in apple juice samples.

## 2. Experimental

### 2.1. Chemicals and instrumentation

Malathion (MAL), triazophos (TRI), chlorpyrifos (CHL), copper(II) nitrate [Cu(NO<sub>3</sub>)<sub>2</sub>], iron(III) nitrate [Fe(NO<sub>3</sub>)<sub>3</sub>], thiourea (THI), MAGA, ethylene glycol dimethacrylate (EGDMA), 2-hydroxyethylmethacrylate (HEMA), AIBN, phosphate buffer (0.1 mol L<sup>-1</sup>, PB) and sodium chloride (NaCl) were bought by Sigma-Aldrich (USA). The apparatus for analytical and structural analysis was given in Supplementary Data.

### 2.2. Preparation of CuFe<sub>2</sub>O<sub>4</sub> and S@CuFe<sub>2</sub>O<sub>4</sub>

Copper ferrites were prepared using a hydrothermal method, initiating with the stirring of 0.20 mol L<sup>-1</sup> Cu(NO<sub>3</sub>)<sub>2</sub> and 0.40 mol L<sup>-1</sup> Fe(NO<sub>3</sub>)<sub>3</sub> solutions for 1 h. Subsequently, a 0.10 mol L<sup>-1</sup> glucose solution was introduced into this mixture and continuously stirred for 24 h at 40 °C. The resulting solution was subjected to the sonication for 1 h before being transferred to an autoclave, where it was held at 160 °C for 5 h. Then, the solution was allowed to cool and filtered using high-grade filter paper to isolate the product (CuFe<sub>2</sub>O<sub>4</sub>).

For the synthesis of S-CuFe<sub>2</sub>O<sub>4</sub>, 1.0 g of CuFe<sub>2</sub>O<sub>4</sub> powder was placed into an autoclave reactor. An appropriate quantity of 1.0% THI solution was then introduced into this mixture. The resulting combination was subsequently treated in the autoclave for 4 h at 160 °C, providing S-CuFe<sub>2</sub>O<sub>4</sub> nanoparticles<sup>26</sup>.

### 2.3. QCM chip modification with S@CuFe<sub>2</sub>O<sub>4</sub> and the preparation of ACE imprinted QCM chip based on S@CuFe<sub>2</sub>O<sub>4</sub>

QCM chips were prepared by cleaning them for 5 min in a conical flask containing 10.0 mL of an acidic piranha solution, which was formulated as a 3:1 (v/v) mixture of sulfuric acid and hydrogen peroxide. Following this cleaning treatment, QCM chips were dried under a protective argon atmosphere. To enable a strong bond between gold surface of QCM chip and sulfur atom of the nanocomposite, S@CuFe<sub>2</sub>O<sub>4</sub> suspension (5.0 mg mL<sup>-1</sup>) was then carefully applied on QCM chip surface. Subsequently, this modified chip (S@CuFe<sub>2</sub>O<sub>4</sub>/QCM) were preserved in an argon atmosphere to prevent the degradation.

Initially, a MAGA-ACE complex solution was prepared by combining the components at a 2:1 molar ratio within 5.0 mL of PB at a pH of 6.0. Subsequently, 4.0 mL of this complex solution was agitated with 2.0 mg of AIBN, 10.0 mL of HEMA, and 10.0 mL of EGDMA to form a polymerization mixture. This mixture was then applied onto the S@CuFe<sub>2</sub>O<sub>4</sub>/QCM chip using spin coating for 10 min, ensuring the formation of a homogeneous, single-layered polymeric structure. Following this, UV polymerization was initiated directly on QCM chip for 10 min, resulting in the production of an ACE-imprinted QCM chip (MIP/S@CuFe<sub>2</sub>O<sub>4</sub>/QCM). Mercury vapor lamp with wavelength range from 315 to 400 nm, emitting a broad spectrum of UV light, was used as a light source and its intensity can range from 10 to 100 mW cm<sup>-2</sup>. For comparative purposes, a non-imprinted QCM chip (NIP/S@CuFe<sub>2</sub>O<sub>4</sub>/QCM) was fabricated using an identical methodology with omitting ACE target molecule.

### 2.4. ACE removal from MIP/S@CuFe<sub>2</sub>O<sub>4</sub>/QCM and analysis process

To effectively dissociate the electrostatic and hydrogen bonding interactions existing between MAGA monomer and ACE analyte, NaCl solution was utilized for the comprehensive removal of ACE. Specifically, MIP/S@CuFe<sub>2</sub>O<sub>4</sub>/QCM chip was submerged

for 10 min in 5.0 mL of a 0.1 mol L<sup>-1</sup> NaCl solution to facilitate the complete elution of ACE molecules. After that, the chip was then subjected to vacuum drying at 25 °C to ensure to eliminate the residual solvent<sup>27</sup>. Once MIP/S@CuFe<sub>2</sub>O<sub>4</sub>/QCM chip, with ACE removed, was integrated into the QCM cell, the system underwent an initial equilibration phase. This involved flushing 3.0 mL of PB with a pH of 6.0 through the QCM cell for 10 min at a constant flow rate of 1.0 mL min<sup>-1</sup>. Following this, the adsorption process was completed using 1.0 mL aliquots of ACE solutions with concentrations varied between 1.0 and 10.0 nmol L<sup>-1</sup>. Each of these ACE solutions was allowed to interact with MIP/S@CuFe<sub>2</sub>O<sub>4</sub>/QCM chip for a duration of 40 min. Subsequently, the desorption phase was initiated by applying 3.0 mL of a 0.1 mol L<sup>-1</sup> NaCl solution over 10-min period. This sequence was completed for a full "adsorption–desorption–regeneration" cycle for each distinct ACE concentration<sup>28</sup>.

### 2.5. Sample preparation

To prepare the apple juice sample for analysis, an initial volume of 5.0 mL was transferred into a 25.0 mL conical flask. This sample then underwent a 10-min centrifugation step to remove any particulate residues. Following residue removal, the solution was diluted with PB with a pH of 6.0 to ensure the target concentration within the detection's linear range. Finally, this diluted sample was introduced into the QCM cell for subsequent analysis.

## 3. Results and discussion

### 3.1. Structural analysis of CuFe<sub>2</sub>O<sub>4</sub> and S@CuFe<sub>2</sub>O<sub>4</sub>

The as-prepared copper ferrite nanostructures were characterized for phase purity and crystalline nature using XRD (Fig. 1A). The analysis of the synthesized nanomaterials revealed prominent diffraction peaks at 18.11°, 29.97°, 35.63°, 36.90°, 43.36°, 53.77°, 57.20°, and 63.12°, which corresponded respectively to the Miller indices of (111), (220), (311), (222), (400), (422), (511), and (440)<sup>29</sup>. XRD patterns definitively confirmed that the synthesized nanomaterials depicted a cubic spinel structure with Fe<sup>3+</sup> ions occupying

1  
2  
3 octahedral sites and  $\text{Cu}^{2+}$  ions occupying tetrahedral positions. Furthermore, while the  
4 presence of sulfur doping led to a notable shift of the major peaks, a decrease in the overall  
5 intensity of the diffraction peaks was observed. XRD patterns, which confirmed the cubic  
6 spinel structure of the synthesized nanomaterials with  $\text{Fe}^{3+}$  ions in octahedral sites and  $\text{Cu}^{2+}$   
7 ions in tetrahedral positions, also clearly indicated the successful replacement of smaller  
8 oxygen ions by larger sulfur anions within  $\text{CuFe}_2\text{O}_4$  structure. Significantly, the absence of  
9  $\text{Fe}_2\text{O}_3$ ,  $\text{FeS}$  or  $\text{CuS}$  crystalline phases indicated the purity of the catalysts, although some  
10 additional peaks beyond  $64.90^\circ$  were observed, suggesting the presence of minor  $\text{CuO}$   
11 content<sup>26, 30</sup>. The distinct sharpness of the observed peaks indicated that the nanomaterials in  
12 this study had a highly crystalline structure.

13  
14  
15  
16  
17  
18  
19  
20  
21  
22  
23  
24  
25  
26  
27  
28  
29  
30  
31  
32  
33  
34  
35  
36  
37  
38  
39  
40  
41  
42  
43  
44  
45  
46  
47  
48  
49  
50  
51  
52  
53  
54  
55  
56  
57  
58  
59  
60

Fig. 1B displayed the FTIR spectra for both  $\text{CuFe}_2\text{O}_4$  and  $\text{S-CuFe}_2\text{O}_4$  nanoparticles. A prominent peak at  $533\text{ cm}^{-1}$  was attributed to M–O vibrational mode of the tetrahedral sites, where M denoted either copper or iron. Additionally, a peak at  $441\text{ cm}^{-1}$  corresponded to the stretching vibrations of the octahedral planes characteristic of these spinel copper oxides. A broad band around  $3490\text{ cm}^{-1}$  suggested O–H bending vibrations, which were associated with hydroxyl groups or water molecules on the nanomaterials' surfaces. Notably, the introduction of sulfur doping caused metal-sulfur vibrations appearing at  $496\text{ cm}^{-1}$ , exhibiting a distinctly lower intensity compared to the Cu–O/Fe–O vibrational peaks. FTIR patterns in the range of  $1025\text{--}1035\text{ cm}^{-1}$  were attributed to C–N stretching vibrations originating from the presence of thiourea<sup>26, 31</sup>. In addition, FTIR spectra of pure  $\text{CuFe}_2\text{O}_4$  could not suggested the nitrogen/carbon (N–C) vibrations.

To examine the physical property changes of the newly synthesized  $\text{S-CuFe}_2\text{O}_4$ , the thermogravimetric analysis (TGA) was conducted (Fig. 1C). These measurements were carried out in a nitrogen atmosphere, spanning a temperature range from  $50\text{ }^\circ\text{C}$  to  $800\text{ }^\circ\text{C}$  at a heating rate of  $5\text{ }^\circ\text{C}/\text{min}$ . The initial analysis revealed a 1.74% mass reduction occurring

below 165 °C, resulting from the evaporation of both adsorbed water and solvent residues. This was a common phenomenon in nanoparticle systems due to their high surface area. The subsequent observations suggested an additional 2.38% decrease in mass as the temperature reached 220 °C, which corresponded to the thermal decomposition of metal hydroxide<sup>32</sup>. These hydroxides were invariably formed during the synthesis of such oxide nanoparticles, particularly when employing precipitation or hydrothermal methods, and their decomposition contributed to the overall weight loss without indicating any organic contamination. After 800 °C, no additional weight loss was detected, indicating the remarkable thermal stability of the S-CuFe<sub>2</sub>O<sub>4</sub> nanoparticles. In addition, this situation suggested the absence of any substantial residual carbonaceous or nitrogenous species that would typically decompose at higher temperatures. In conclusion, 4.12% mass reduction was not to the contamination by residual carbon/nitrogen species from incomplete THI decomposition.

**Here Fig. 1.**

SEM was employed to examine the morphological characteristics of both pristine S@CuFe<sub>2</sub>O<sub>4</sub> and CuFe<sub>2</sub>O<sub>4</sub> nanostructures. The observations revealed that CuFe<sub>2</sub>O<sub>4</sub> nanoparticles exhibited an agglomerated state, displaying irregular and flake-like formations. This tendency for CuFe<sub>2</sub>O<sub>4</sub> nanoparticles was attributed to the agglomeration in clusters due to the attractive forces (Fig. 2A)<sup>33</sup>. In addition, Fig. 2B revealed that sulfur doping caused a more regular flake-like morphology and a noticeable reduction in agglomeration, providing the evidence for increased nanomaterial porosity<sup>34</sup>. Consequently, the availability of active sites increased. These findings suggested that sulfur doping improved the surface area and thus contributed to an enhanced adsorption activity of CuFe<sub>2</sub>O<sub>4</sub> nanoparticles. EDX results also demonstrated the presence of copper, iron, oxygen and sulphur, confirming the successful synthesis of S@CuFe<sub>2</sub>O<sub>4</sub> (Fig. S1). Finally, XPS experiment was accomplished to examine the attachment of sulphur to the gold surface of QCM chip. The S2p region displayed a

doublet, specifically the 2p<sub>1/2</sub> and 2p<sub>3/2</sub> orbitals, due to the inherent spin-orbit coupling. The presence of sulphur peaks at 168.13 eV on S@CuFe<sub>2</sub>O<sub>4</sub>/QCM chip suggested that its sulphur readily formed a bond with the gold surface of the QCM chip. Furthermore, an additional peak observed at 163.06 eV served as an indicator for the existence of a free mercapto group within the system (Fig. S2).<sup>35</sup>

Here Fig. 2.

### 3.2. FTIR and AFM analysis of ACE-imprinted film on S@CuFe<sub>2</sub>O<sub>4</sub>/QCM

Following the removal of ACE, FTIR spectroscopy was performed on ACE-imprinted film on S@CuFe<sub>2</sub>O<sub>4</sub>/QCM, revealing characteristic absorption peaks. Specifically, the distinct bands were observed at 3618 cm<sup>-1</sup> corresponding to the hydroxyl stretching vibrations of both MAGA and HEMA monomers; at 2991 cm<sup>-1</sup> indicating –CH bond stretching; at 1760 cm<sup>-1</sup> associated with carboxyl-carbonyl stretching; and at 1486 cm<sup>-1</sup> reflecting –COO– stretching (Fig. S3A). The consistent presence of these specific spectral peaks validated the successful formation of ACE-imprinted film on S@CuFe<sub>2</sub>O<sub>4</sub>/QCM. Furthermore, AFM images (Fig. S3B and Fig. S3C) presented the varying surface morphologies of a pristine QCM chip in comparison with ACE-imprinted film on S@CuFe<sub>2</sub>O<sub>4</sub>/QCM. The quantitative analysis from AFM measurements produced an average thickness of 3.07±0.14 nm for the bare QCM chip and a greater average thickness of 27.79±0.09 nm for ACE-imprinted film on S@CuFe<sub>2</sub>O<sub>4</sub>/QCM. These substantial differences in film thickness provide an important evidence for the successful formation of ACE-imprinted polymeric layers on QCM chip's surface.

### 3.3. pH effect on ACE-imprinted film on S@CuFe<sub>2</sub>O<sub>4</sub>/QCM and the modification effect

Due to MAGA monomer having two pKa values (pKa1=2.10 and pKa2=4.07), the acidic MAGA monomer depicted minimal ionization under acidic pH conditions, providing the limited interaction with ACE. However, as the pH increased, the carboxylic acid groups of

MAGA monomer became negatively. Consequently, these negative groups interacted with NH groups of ACE.<sup>36</sup> Conversely, owing to the concentration of the anion form of ACE increased under alkaline conditions (i.e., pH greater than 7.0), the interaction between the monomer and ACE diminished. This reduction was attributed to the electrostatic repulsion lowering their binding affinity on the QCM chip surface. As depicted in Fig. 3A, the most robust interaction between the monomer and the analyte was observed at a pH of 6.0. Therefore, this specific pH level was designated as the optimal condition for all subsequent analytical methodologies<sup>37</sup>.

Fig. 3B revealed the important impact of surface modification on QCM sensor signals when exposed to 5.0 nmol L<sup>-1</sup> ACE. A low QCM sensor response ( $\Delta m=2.0$  ng cm<sup>-2</sup>) was observed when using a MIP/QCM (curve a of Fig. 3B). Then, a substantial increase in QCM sensor signal was observed on curve b of Fig. 3B when using MIP/S@CuFe<sub>2</sub>O<sub>4</sub>/QCM. The reasons for this large mass change caused by S@CuFe<sub>2</sub>O<sub>4</sub> could be listed as follows. (i) this marked enhancement was ascribed to the formation of highly stable self-assembled monolayers, resulting from the strong sulphur-gold covalent bonds<sup>38</sup> and sulphur doping providing the increased porosity<sup>34</sup>. (ii) sulphur doping could alter the electronic band structure of CuFe<sub>2</sub>O<sub>4</sub>. This change provided more favorable interactions with specific ACE target<sup>39</sup>. (iii) sulphur doping often introduced defects into the crystal lattice. These defects could act as the enhanced adsorption sites, increasing the binding affinity and potentially the selectivity for ACE molecules. The creation of more active and specific adsorption sites due to sulphur doping could lead to a higher quantity of the adsorbed ACE molecules onto the S@CuFe<sub>2</sub>O<sub>4</sub> film.<sup>40</sup> (iv) sulphur doping could lead to an improvement in the structural stability of the sensing material, making the QCM sensor more robust in challenging environments<sup>41</sup>. Finally, as expected, smaller mass change values were observed when using MIP/CuFe<sub>2</sub>O<sub>4</sub>/QCM without sulphur doping (curve c of Fig. 3B). Thus, these advanced monolayers played a

crucial role in generating more binding site enhancement between S@CuFe<sub>2</sub>O<sub>4</sub> and ACE molecule, consequently leading to a significant improvement in the sensor response and performance.

Here Fig. 3.

### 3.4. Sensitivity of MIP/S@CuFe<sub>2</sub>O<sub>4</sub>/QCM

The analytical performance of MIP/S@CuFe<sub>2</sub>O<sub>4</sub>/QCM chip was characterized through QCM sensorgrams, as presented in Fig. 4A. These sensorgrams were obtained from QCM responses across a broad ACE concentration range from 1.0 to 10.0 nmol L<sup>-1</sup>. From these results, a robust linear relationship was established between MIP/S@CuFe<sub>2</sub>O<sub>4</sub>/QCM sensor signals and the corresponding ACE concentrations (Fig. 4B). This relationship produced a precise calibration equation of  $y \text{ (ng cm}^{-2}\text{)} = 0.9940x(\text{C}_{\text{ACE}}, \text{nmol L}^{-1}\text{)} - 0.0891$ . This equation effectively quantified QCM sensor's analytical ability, showing its reliability for ACE detection within the specified concentration range. The MIP/S@CuFe<sub>2</sub>O<sub>4</sub>/QCM sensor demonstrated remarkable analytical sensitivity, achieving a limit of quantification (LOQ) of  $1.0 \times 10^{-9} \text{ mol L}^{-1}$  and a LOD of  $3.30 \times 10^{-10} \text{ mol L}^{-1}$ , thereby confirming its robust performance (with detailed equations provided in the supplementary data) in comparison with the other methods (Table 1). While chromatographic techniques such as LC-MS and GC-MS were employed for ACE determination<sup>42-44</sup>, these methods raised important environmental concerns owing to the excessive usage of chemical agents. In contrast, this study's approach, which incorporated a hydrothermal method for S@CuFe<sub>2</sub>O<sub>4</sub> nanocomposite, significantly minimized waste generation. Therefore, MIP/S@CuFe<sub>2</sub>O<sub>4</sub>/QCM system offered a rapid detection platform for critical metabolic disorders resulting from exposure to potent pesticides.

Here Fig. 4.

**Table 1.** The comparison of MIP/S@CuFe<sub>2</sub>O<sub>4</sub>/QCM sensor with the studied methods for ACE detection

Method/Material	Linear range (mol L <sup>-1</sup> )	LOD (mol L <sup>-1</sup> )	Ref.
Boron-nitrogen co-doped carbon dots	0.0 – 1.0×10 <sup>-6</sup>	2.70×10 <sup>-8</sup>	45
AgNPs-ZnO/SERS	6.0×10 <sup>-9</sup> – 8.0×10 <sup>-7</sup>	3.40×10 <sup>-9</sup>	46
Amperometric biosensor	1.0×10 <sup>-7</sup> – 1.0×10 <sup>-2</sup>	1.0×10 <sup>-9</sup>	47
Fluorometric method	2.7×10 <sup>-8</sup> – 4.4×10 <sup>-7</sup>	1.99×10 <sup>-8</sup>	48
Cyclic voltammetry	5.57×10 <sup>-7</sup> – 4.6×10 <sup>-6</sup>	2.40×10 <sup>-7</sup>	49
Colorimetric method	1.0×10 <sup>-8</sup> – 2.73×10 <sup>-6</sup>	6.0×10 <sup>-8</sup>	50
MIP/S@CuFe <sub>2</sub> O <sub>4</sub> /QCM	1.0×10 <sup>-9</sup> – 1.0×10 <sup>-8</sup>	3.30×10 <sup>-10</sup>	This study

### 3.5. Recovery

To confirm the effectiveness of MIP/S@CuFe<sub>2</sub>O<sub>4</sub>/QCM chip, the recovery assessments were conducted within apple juice samples. The results, detailed in Table 2, revealed a high recovery rate of nearly 100.00%. This high percentage suggested the sensor's high precision and its capacity to ACE analyte even in complex matrix interference. Furthermore, the detection of ACE in apple juice was carried out using the application of LC-MS/MS<sup>51</sup>. As detailed in Table 2, the data indicated a strong correlation between the measurements acquired using MIP/S@CuFe<sub>2</sub>O<sub>4</sub>/QCM chip and LC-MS/MS technique and an important difference between the results of two methods was not found (Wilcoxon test:  $T_{\text{calculated}} > T_{\text{tabulated}}, p > 0.05$ ).

To further validate the sensor's analytical capabilities, the standard addition method was employed for ACE quantification in apple juice samples, yielding a calibration equation of  $y \text{ (ng cm}^{-2}\text{)} = 0.9972x \text{ (C}_{\text{ACE}}, \text{ nmol L}^{-1}\text{)} - 0.1973$ . The remarkable harmony between the slopes derived from this standard addition calibration and the direct calibration equation was an important indicator of the developed sensor's high specificity in complex matrix interferences.



**Table 2.** Recovery results of ACE ( $n=6$ )View Article Online  
DOI: 10.1039/D6AY00590J

Sample	MIP/S@CuFe <sub>2</sub> O <sub>4</sub> /QCM			LC-MS/MS	
	Added ACE (nmol L <sup>-1</sup> )	Found ACE (nmol L <sup>-1</sup> )	*Recovery (%)	Found ACE (nmol L <sup>-1</sup> )	*Recovery (%)
Apple juice	-	0.76 ± 0.02	-	0.75 ± 0.03	-
	2.00	2.77 ± 0.06	100.36 ± 0.06	2.74 ± 0.04	99.64 ± 0.03
	5.00	5.75 ± 0.04	99.83 ± 0.01	5.76 ± 0.02	100.17 ± 0.08
	8.00	8.74 ± 0.03	99.77 ± 0.01	8.76 ± 0.05	100.11 ± 0.05

\*Recovery = Found ACE, nmol L<sup>-1</sup> / Real ACE, nmol L<sup>-1</sup>**3.6. Stability, selectivity, repeatability, and reproducibility of MIP/S@CuFe<sub>2</sub>O<sub>4</sub>/QCM**

The stability of the novel sensor was confirmed through an 8-week evaluation of a single MIP/S@CuFe<sub>2</sub>O<sub>4</sub>/QCM chip. During this period, QCM sensorgrams were consistently recorded using a 5.0 nmol L<sup>-1</sup> ACE solution. Remarkably, the QCM signal observed at the conclusion of the 8<sup>th</sup> week retained approximately 99.36% of the initial signal measured at the end of the first week, definitively demonstrating the high operational stability of this innovative sensing platform.

The selectivity studies in the presence of structurally similar organophosphorus pesticides such as MAL, TRI and CHL were completed using MIP/S@CuFe<sub>2</sub>O<sub>4</sub>/QCM towards ACE<sup>47</sup>. The MIP/S@CuFe<sub>2</sub>O<sub>4</sub>/QCM chip demonstrated superior selectivity towards ACE analyte. This superior selectivity was verified by exposing MIP/S@CuFe<sub>2</sub>O<sub>4</sub>/QCM chip to a 5.0 nmol L<sup>-1</sup> concentration of ACE and the interfering substances such as MAL, TRI, and CHL (Fig. 5A). The results suggested the sensor's selectivity to bind ACE in the presence of a substantial excess of other compounds, highlighting its robustness for selective detection. Subsequently, the quantification of both selectivity ( $k$ ) and relative selectivity ( $k'$ ) coefficients was evaluated (Table S1). These calculations showed that MIP/S@CuFe<sub>2</sub>O<sub>4</sub>/QCM chip exhibited superior selectivity for the ACE analyte, proving to be 18.33 times more selective than for MAL, 27.50 times more selective than for TRI, and 55.00 times more selective than for CHL. Furthermore, Fig. 5B demonstrated the remarkable selectivity achieved through the



molecular imprinting technology when compared against the non-imprinted polymer (NIP/S@CuFe<sub>2</sub>O<sub>4</sub>/QCM) chip. The  $k'$  values greater than 1, which ranged from 2.75 to 3.67 (as indicated in Table S1), confirmed the MIP/S@CuFe<sub>2</sub>O<sub>4</sub>/QCM chip's high selectivity for detecting ACE.

**Here Fig. 5.**

The repeatability of an individual MIP/S@CuFe<sub>2</sub>O<sub>4</sub>/QCM chip was evaluated by conducting five successive "adsorption–desorption–regeneration" cycles, each utilizing a 5.0 nmol L<sup>-1</sup> ACE solution. Across all five cycles, the highly consistent QCM signals with approximately 5.50 ng cm<sup>-2</sup> belonging to a relative standard deviation (RSD) of 0.62% were recorded (as illustrated in Fig. S4). This consistent performance indicated the superior repeatability of MIP/S@CuFe<sub>2</sub>O<sub>4</sub>/QCM chip, highlighting its reliability for the repeated measurements.

To establish the reproducibility of the sample preparation method, 25 individual MIP/S@CuFe<sub>2</sub>O<sub>4</sub>/QCM chips were fabricated at same batches via the procedures described in Sect. 2.3. The manufactured chips were stored in a sealed environment at 25 °C to protect them from temperature and pressure changes, interfering with the crystal's natural resonance. In addition, MIP/S@CuFe<sub>2</sub>O<sub>4</sub>/QCM chips could be oriented horizontally. Each of these independent chips was subsequently exposed to 5.0 nmol L<sup>-1</sup> ACE. The analysis of the QCM signals obtained from these 25 separate QCM chips produced a RSD of 0.89%. This low value for RSD indicated the high reproducibility in QCM sensor fabrication procedure.

**3.7. Ruggedness and robustness of MIP/S@CuFe<sub>2</sub>O<sub>4</sub>/QCM**

The ruggedness and robustness experiments of MIP/S@CuFe<sub>2</sub>O<sub>4</sub>/QCM chip were evaluated with Wilcoxon test statistical analyses. To assess ruggedness, the influence of different researchers on the sensor's performance was investigated when analyzing 5.0 nmol L<sup>-1</sup> ACE and the absence of a statistically significant difference ( $p > 0.05$ ) clearly demonstrated

the sensor's excellent reliability across various operators. Similarly, the robustness of the sensor was confirmed by examining the impact of slight variations from the optimal pH (specifically at pH 5.9 and pH 6.1). The test also revealed no significant variation ( $p > 0.05$ ), thereby demonstrating the sensor's high tolerance to minor changes in environmental conditions.

### 3.8. Greenness evaluation

The environmental compatibility of the MIP/S@CuFe<sub>2</sub>O<sub>4</sub>/QCM chip was assessed using both the Green Analytical Procedure Index (GAPI) and Analytical GREENness (AGREE). GAPI's visual pictograms, utilizing a green, yellow, and red light system, provided a comprehensive overview of all functionalities associated with the MIP/S@CuFe<sub>2</sub>O<sub>4</sub>/QCM chip. Furthermore, the AGREE score, ranging from 0.0 to 1.0, yielded a result of 0.91. This robust score indicated the green nature of the methodology employed (Fig. S5 and Fig. S6) confirming the high practical applicability of the MIP/S@CuFe<sub>2</sub>O<sub>4</sub>/QCM chip and its associated tools.

## 4. Conclusion

A new QCM sensor, combining a molecularly imprinted polymer with sulfur-doped copper ferrites, was developed for the accurate detection of acephate pesticide in apple juice. This advanced sensor revealed high selectivity, and sensitivity. It showed a linear detection range spanning from  $1.0 \times 10^{-9}$  to  $1.0 \times 10^{-8}$  mol L<sup>-1</sup> with a low detection limit of  $3.30 \times 10^{-10}$  mol L<sup>-1</sup>. Furthermore, experimental data revealed high recovery rates, falling within the narrow margin of 99.77 to 100.36%. High stability, repeatability, and reproducibility of the proposed sensor were verified. Finally, the proven efficacy of QCM sensor based on hydrothermally synthesized sulfur-doped copper ferrites in practical applications indicated its promising potential for future identification of a wider array of pesticide residues.

### Data availability

The original data in this study are included in the manuscript, and further inquiries can be directed to the corresponding author.

### Conflicts of interest

There are no conflicts to declare.

### References

1. Z. Lin, S. Pang, W. Zhang, S. Mishra, P. Bhatt and S. Chen, *Front Microbiol*, 2020, **11**, 2045.
2. K. Rahila and Y. Shibu Vardhanan, *Pestic Biochem Physiol*, 2024, **203**, 106023.
3. J. Jurewicz and W. Hanke, *Int J Occup Med Environ Health*, 2006, **19**, 152-169.
4. S. R. Ruberu, W. M. Draper and S. K. Perera, *J Agric Food Chem*, 2000, **48**, 4109-4115.
5. M. Petrovic, M. D. Hernando, M. S. Diaz-Cruz and D. Barcelo, *J Chromatogr A*, 2005, **1067**, 1-14.
6. R. Singh, R. Gupta, D. Bansal, R. Bhateria and M. Sharma, *ACS Omega*, 2024, **9**, 7336-7356.
7. B. Kong, A. Zhu, C. Ding, X. Zhao, B. Li and Y. Tian, *Adv Mater*, 2012, **24**, 5844-5848.
8. M. R. Patil, S. D. Subhash D. Khairnar and D. Shrivastava, *Appl Nanosci*, 2016, **6**, 495-502.
9. R. R. Ding, Li, W. Q., He, C. S., Wang, Y. R., Liu, X. C., Zhou, G. N., and Mu, Y., *Appl Catal B-Environ*, 2021, **291**, 120069.
10. M. S. Amulya, H. P. Nagaswarupa, M. A. Kumar, C. R. Ravikumar, K. B. Kusuma, and S. C. Prashantha, *J Phys Chem Solids*, 2021, **148**, 109756.
11. N. Maji and H. S. Dosanjh, *Magnetochemistry*, 2023, **9**, 156.
12. S. P. Keerthana, R. Yuvakkumar, G. Ravi, S. Pavithra, M. Thambidurai, C. Dang and D. Velauthapillai, *Environ Res*, 2021, **200**, 111528.
13. A. B. Patil, K. R. Patil and S. K. Pardeshi, *J Hazard Mater*, 2010, **183**, 315-323.
14. C. S. Meric, B. B. Yola, S. Bekerecioglu, I. Polat, N. Atar and M. L. Yola, *Microchim Acta*, 2026, **193**, 55.
15. B. Bankoğlu Yola, S. Bekerecioglu, İ. Polat, U. M. Alptekin, N. Atar, and M. L. Yola, *Foods*, 2026, **15**, 7.
16. S. Harmankaya, H. A. Deveci, A. Harmankaya, F. H. Gul, N. Atar and M. L. Yola, *Biosensors*, 2024, **14**.

- 1  
2  
3  
4  
5  
6  
7  
8  
9  
10  
11  
12  
13  
14  
15  
16  
17  
18  
19  
20  
21  
22  
23  
24  
25  
26  
27  
28  
29  
30  
31  
32  
33  
34  
35  
36  
37  
38  
39  
40  
41  
42  
43  
44  
45  
46  
47  
48  
49  
50  
51  
52  
53  
54  
55  
56  
57  
58  
59  
60
17. M. A. Erbağcı, K. Kaplan, N. Atar and M. L. Yola, *Microchem J*, 2026, **224**, 117880. Article Online  
DOI: 10.1039/D6AY00590J
18. M. A. Erbağcı, K. Kaplan, N. Özdemir, H. E. Altınok and M. L. Yola, *Microchim Acta*, 2026, **193**.
19. F. H. Gul, H. A. Deveci, A. Deveci, O. Akyıldırım and M. L. Yola, *Microchim Acta*, 2025, **192**, 124.
20. S. Harmankaya, H. A. Deveci, A. Harmankaya, F. H. Gül, N. Atar and M. L. Yola, *Microchim Acta*, 2025, **192**, 729.
21. Ş. Y. Akıcı, S. Bekerecioğlu, İ. Polat, M. M. Kaya, N. Atar and M. L. Yola, *Microchim Acta*, 2025, **192**, 867.
22. Ç. S. Meriç, H. A. Deveci, M. M. Kaya, A. Deveci, N. Özdemir, H. Boyacıoğlu and M. L. Yola, *Anal Methods*, 2025, **17**, 1080-1089.
23. B. Bankoğlu Yola, N. Özdemir and M. L. Yola, *Biosensors*, 2024, **14**, 571.
24. M. L. Yola, *Chemosphere*, 2022, **301**, 134766.
25. N. Özcan, H. Medetalibeyoglu, O. Akyıldırım, N. Atar and M. L. Yola, *Mater Today Commun*, 2020, **23**, 101097.
26. A. Aslam, M. Z. Abid, K. Rafiq, A. Rauf and E. Hussain, *Sci Rep*, 2023, **13**, 6306.
27. M. Mavioglu Kaya, H. A. Deveci, B. Bankoglu Yola, I. Polat, S. Bekerecioglu, N. Atar and M. L. Yola, *Foods*, 2026, **15**.
28. Ş. Y. Akıcı, A. Duzel, U. M. Alptekin, S. Bekerecioglu, I. Polat, N. Atar and M. L. Yola, *Anal Methods*, 2026, **18**, 1331-1339.
29. G. Sreekala, A. F. Beevi, R. Resmi, and B. Beena, *Mater Today: Proc*, 2021, **45**, 3986-3990.
30. K. M. Rezaul Karim, M. Tarek, H. R. Ong, H. Abdullah, A. Yousuf, C. K. Cheng, and M. M. R Khan, *Ind. Eng. Chem. Res*, 2018, **58**, 563-572.
31. Z. Mirzaeifard, Z. Shariatnia, M. Jourshabani and S. M. Rezaei Darvishi, *Ind Eng Chem Res*, 2020, **59**, 15894-15911.
32. L. Luo, R. Cui, H. Qiao, K. Chen, Y. Fei, D. Li, Z. Pang, K. Liu and Wei, Q., *Electrochim Acta*, 2014, **144**, 85-91.
33. P. Hoa, N.P. Duong, T.T. Loan, L.N. Anh and N.M. Hong, *Vietnam J Chem*, 2019, **57**, 32-38.
34. T. Oliveira, S.F. Rodrigues, G.N. Marques, R.C.V. Costa, C.G.G. Lopes, C. Aranas, A. Rojas, J.H.G. Rangel and M.M. Oliveira, *Catalysts*, 2022, **12**, 623.

- 1  
2  
3 35. M. L. Yola, N. Atar, Z. Üstündağ and A. O. Solak, *J Electroanal Chem*, 2013, **698**, 9  
4 16. Article Online  
DOI: 10.1039/D6AY00590J
- 5  
6 36. M. L. Yola, L. Uzun, N. Özaltın and A. Denizli, *Talanta*, 2014, **120**, 318-324.
- 7  
8 37. S. Kadirsoy, N. Atar and M. L. Yola, *New J Chem*, 2020, **44**, 6524-6532.
- 9  
10 38. X. Luo, Y. Fan, , X. Li, Y. Zhang, J. Chen and P. Li, *Chem Eng J*, 2025, **521**, 166989.
- 11  
12 39. E. Hussain, A. K. Buzdar, M. Z. Abid, A. Rauf and K. Rafiq, *J. Environ. Manage.*,  
13 2024, **370**, 122759.
- 14  
15 40. C. Xiunan, T. Ling, C. Meifei, L. Yijun, W. Wei, L. Junhao, Z. Yanjuan, T. Gan, H.  
16 Huayu and H. Zuqiang, *Chemosphere*, 2022, **296**, 134005.
- 17  
18 41. C. Wang, S.-H. Zhang, L. Zhang, R. Xi, D.-P. Jiang, Z.-Y. Chen, H. Huang, L.-Y.  
19 Ding and G.-B. Pan, *J. Power Sources*, 2019, **443**, 227183.
- 20  
21 42. A. D. St-Amand and L. Girard, *Int J. Environ Anal Chem*, 2004, **84**, 739-748.
- 22  
23 43. L. Oka-Duarte, A.A vila and de A. R. M. Oliveira, *Microchem J*, 2025, **215**, 114306.
- 24  
25 44. X. Wang, H. Zhang, H. Xu, P. Qi, X. Ji, Q. Wang and X. Wang, *Food Anal Meth*  
26 2013, **6**, 133–140.
- 27  
28 45. A. Mallik, M. Hazra, M. K. Adak, R. Nag, A. Pandey and G. P. Sahoo, *Diam Relat*  
29 *Mater*, 2025, **153**, 112107.
- 30  
31 46. L. Niu, X. Wang, X. Liu, X. Liu, S. Niu, B. Yang and S. Bi, *J Lumin*, 2026, **293**,  
32 121796.
- 33  
34 47. B. Patial, M. Pabbi, S.Gupta, S. K. Mittal, A. Bansal and R. Gupta, *Bioresour Technol*  
35 *Rep*, 2025, **31**, 102278.
- 36  
37 48. P. Singh, S. Kumar and S. K. Verma, *Talanta*, 2023, **252**, 123843.
- 38  
39 49. P. Raghu, T. Madhusudana Reddy, K. Reddaiah, B. E. Kumara Swamy and M.  
40 Sreedhar, *Food Chem*, 2014, **142**, 188-196.
- 41  
42 50. M. J. Osman, J. I. Abdul Rashid, O. K. Khim, W. M. Zin Wan Yunus, S. A. Mohd  
43 Noor, N. A. Mohd Kasim, V. F. Knight and T. C. Chuang, *RSC Adv*, 2021, **11**, 25933-  
44 25942.
- 45  
46 51. E. M. Brovini, M. E. P. Martucci, M. de Oliveira, A. H. S. Oliveira and S. F. de  
47 Aquino, *Int J. Environ Anal Chem*, 2025, **105**, 2782-2797.
- 48  
49  
50  
51  
52  
53  
54  
55  
56  
57  
58  
59  
60

**Figure Caption**View Article Online  
DOI: 10.1039/D6AY00590J

**Fig. 1.** (A) XRD patterns of S@CuFe<sub>2</sub>O<sub>4</sub> and CuFe<sub>2</sub>O<sub>4</sub>, (B) FTIR spectrum of S@CuFe<sub>2</sub>O<sub>4</sub> and CuFe<sub>2</sub>O<sub>4</sub> and (C) TGA curve of S@CuFe<sub>2</sub>O<sub>4</sub>

**Fig. 2.** SEM images of (A) CuFe<sub>2</sub>O<sub>4</sub> and (B) S@CuFe<sub>2</sub>O<sub>4</sub>

**Fig. 3.** (A) QCM sensorgrams for 5.0 nmol L<sup>-1</sup> ACE in different pHs of PB and (B) QCM sensorgrams on MIP/QCM (curve a), MIP/S@CuFe<sub>2</sub>O<sub>4</sub>/QCM (curve b) and MIP/CuFe<sub>2</sub>O<sub>4</sub>/QCM (curve c) in presence of 5.0 nmol L<sup>-1</sup> ACE

**Fig. 4.** (A) QCM sensorgrams with different ACE concentration on MIP/S@CuFe<sub>2</sub>O<sub>4</sub>/QCM chip in existence of pH 6.0 of PB (from 1.0 nmol L<sup>-1</sup> to 10.0 nmol L<sup>-1</sup> ACE) and (B) Calibration curve of ACE concentrations against QCM signals

**Fig. 5.** Selectivity studies at (A) MIP/S@CuFe<sub>2</sub>O<sub>4</sub>/QCM chip and (B) NIP/S@CuFe<sub>2</sub>O<sub>4</sub>/QCM chip in 5.0 nmol L<sup>-1</sup> ACE, 5.0 nmol L<sup>-1</sup> MAL, 5.0 nmol L<sup>-1</sup> TRI, and 5.0 nmol L<sup>-1</sup> CHL

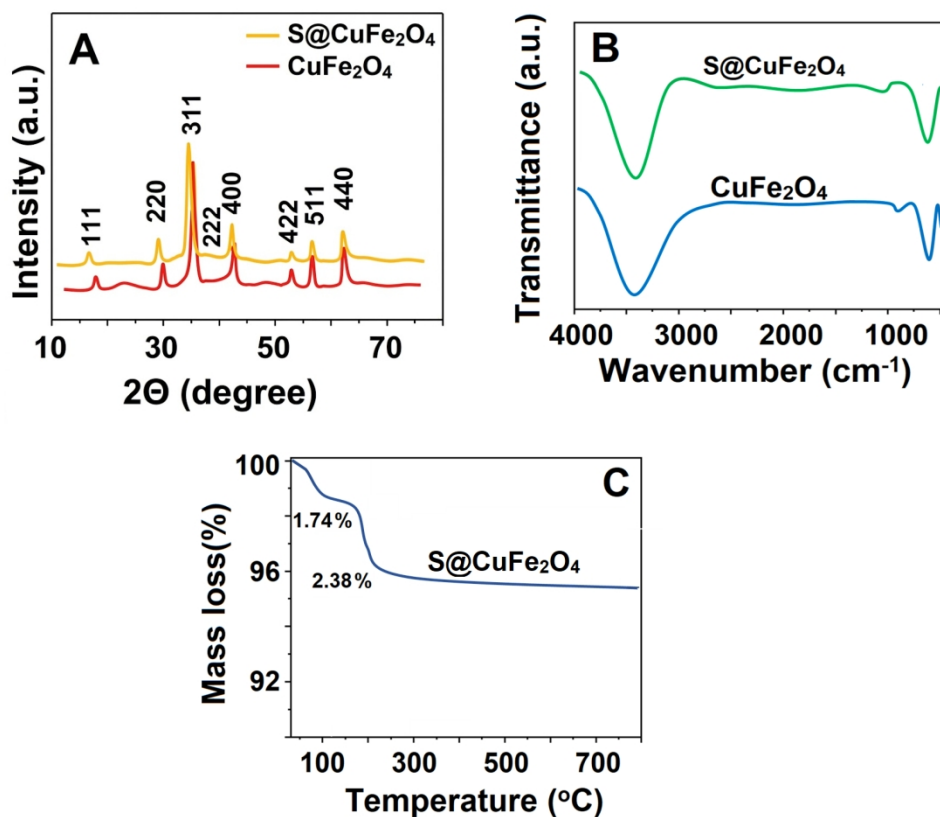


Fig. 1. (A) XRD patterns of S@CuFe<sub>2</sub>O<sub>4</sub> and CuFe<sub>2</sub>O<sub>4</sub>, (B) FTIR spectrum of S@CuFe<sub>2</sub>O<sub>4</sub> and CuFe<sub>2</sub>O<sub>4</sub> and (C) TGA curve of S@CuFe<sub>2</sub>O<sub>4</sub>

390x324mm (120 x 120 DPI)

1  
2  
3  
4  
5  
6  
7  
8  
9  
10  
11  
12  
13  
14  
15  
16  
17  
18  
19  
20  
21  
22  
23  
24  
25  
26  
27  
28  
29  
30  
31  
32  
33  
34  
35  
36  
37  
38  
39  
40  
41  
42  
43  
44  
45  
46  
47  
48  
49  
50  
51  
52  
53  
54  
55  
56  
57  
58  
59  
60

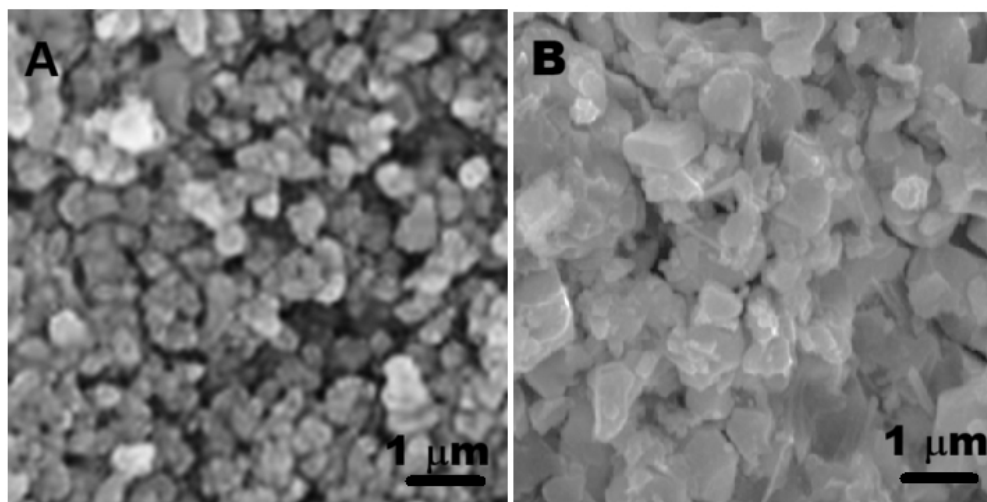


Fig. 2. SEM images of (A) CuFe<sub>2</sub>O<sub>4</sub> and (B) S@CuFe<sub>2</sub>O<sub>4</sub>

189x96mm (96 x 96 DPI)



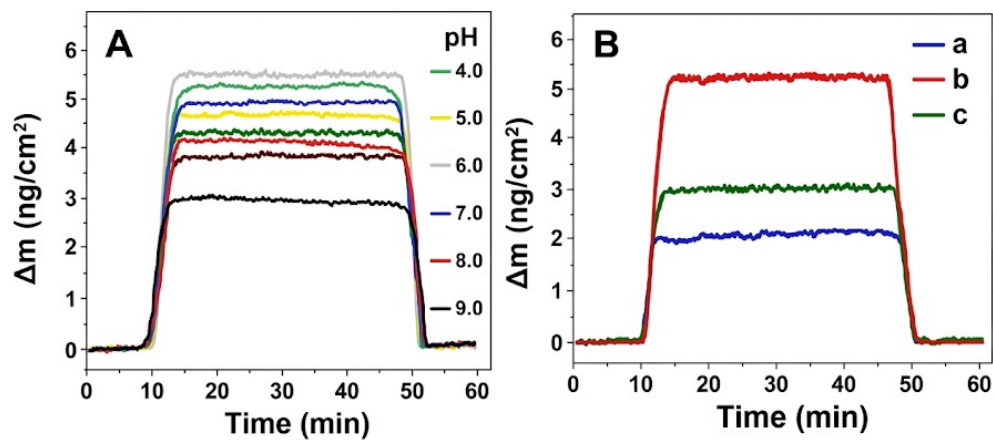


Fig. 3. (A) QCM sensorgrams for 5.0 nmol L-1 ACE in different pHs of PB and (B) QCM sensorgrams on MIP/QCM (curve a), MIP/S@CuFe<sub>2</sub>O<sub>4</sub>/QCM (curve b) and MIP/CuFe<sub>2</sub>O<sub>4</sub>/QCM (curve c) in presence of 5.0 nmol L-1 ACE

190x84mm (120 x 120 DPI)

1  
2  
3  
4  
5  
6  
7  
8  
9  
10  
11  
12  
13  
14  
15  
16  
17  
18  
19  
20  
21  
22  
23  
24  
25  
26  
27  
28  
29  
30  
31  
32  
33  
34  
35  
36  
37  
38  
39  
40  
41  
42  
43  
44  
45  
46  
47  
48  
49  
50  
51  
52  
53  
54  
55  
56  
57  
58  
59  
60

Downloaded on 5/4/2024 6:32:37 PM.  
Creative Commons Attribution-NonCommercial 3.0 Unported Licence.



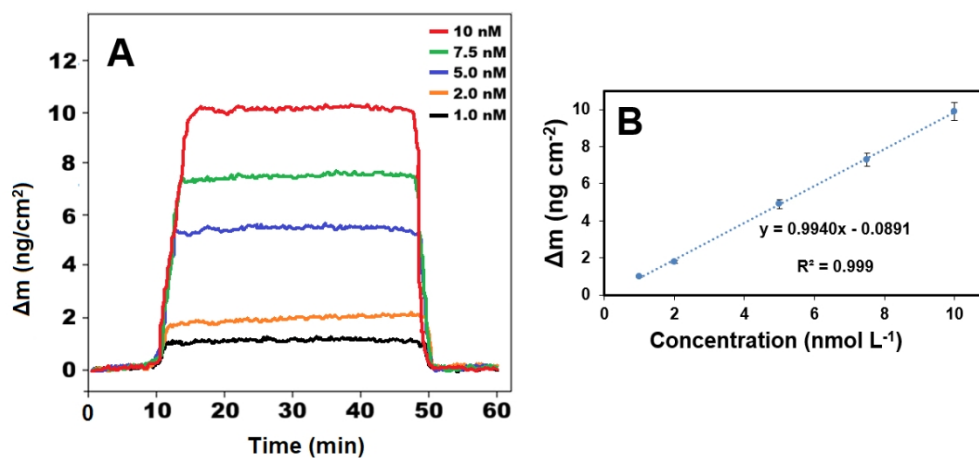


Fig. 4. (A) QCM sensorgrams with different ACE concentration on MIP/S@CuFe<sub>2</sub>O<sub>4</sub>/QCM chip in existence of pH 6.0 of PB (from 1.0 nmol L<sup>-1</sup> to 10.0 nmol L<sup>-1</sup> ACE) and (B) Calibration curve of ACE concentrations against QCM signals

323x147mm (96 x 96 DPI)

1  
2  
3  
4  
5  
6  
7  
8  
9  
10  
11  
12  
13  
14  
15  
16  
17  
18  
19  
20  
21  
22  
23  
24  
25  
26  
27  
28  
29  
30  
31  
32  
33  
34  
35  
36  
37  
38  
39  
40  
41  
42  
43  
44  
45  
46  
47  
48  
49  
50  
51  
52  
53  
54  
55  
56  
57  
58  
59  
60

Downloaded on 5/4/2022 6:32:37 PM.  
This article is licensed under a Creative Commons Attribution-NonCommercial 3.0 Unported Licence.



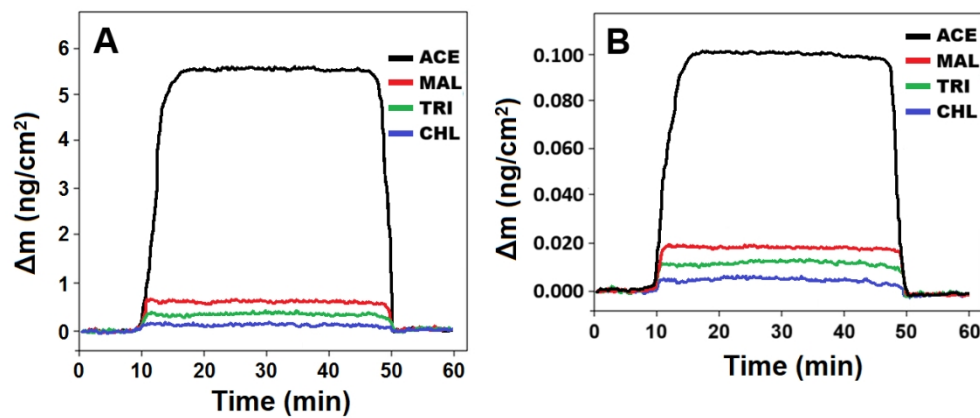


Fig. 5. Selectivity studies at (A) MIP/S@CuFe<sub>2</sub>O<sub>4</sub>/QCM chip and (B) NIP/S@CuFe<sub>2</sub>O<sub>4</sub>/QCM chip in 5.0 nmol L-1 ACE, 5.0 nmol L-1 MAL, 5.0 nmol L-1 TRI, and 5.0 nmol L-1 CHL

352x146mm (96 x 96 DPI)

1  
2  
3  
4  
5  
6  
7  
8  
9  
10  
11  
12  
13  
14  
15  
16  
17  
18  
19  
20  
21  
22  
23  
24  
25  
26  
27  
28  
29  
30  
31  
32  
33  
34  
35  
36  
37  
38  
39  
40  
41  
42  
43  
44  
45  
46  
47  
48  
49  
50  
51  
52  
53  
54  
55  
56  
57  
58  
59  
60

Downloaded on 5/4/2022 6:32:37 PM.  
This article is licensed under a Creative Commons Attribution-NonCommercial 3.0 Unported Licence.



The original data in this study are included in this study, and further inquiries can be directed to the corresponding author.

View Article Online  
DOI: 10.1039/D6AY00590J

Analytical Methods Accepted Manuscript

1  
2  
3  
4  
5  
6  
7  
8  
9  
10  
11  
12  
13  
14  
15  
16  
17  
18  
19  
20  
21  
22  
23  
24  
25  
26  
27  
28  
29  
30  
31  
32  
33  
34  
35  
36  
37  
38  
39  
40  
41  
42  
43  
44  
45  
46  
47  
48  
49  
50  
51  
52  
53  
54  
55  
56  
57  
58  
59  
60

Open Access Article. Published on 04 May 2026. Downloaded on 5/4/2026 8:32:37 PM.  
This article is licensed under a Creative Commons Attribution-NonCommercial 3.0 Unported Licence.

